phys. stat. sol. (a) **205**, No. 12, 2796–2810 (2008) / **DOI** 10.1002/pssa.200880455

physica status solidi a
www.pss-a.com
applications and materials science

3D photonic crystal intermediate reflector for micromorph thin-film tandem solar cell

Andreas Bielawny[*,1], Johannes Üpping[1], Paul T. Miclea[1], Ralf B. Wehrspohn[1],Carsten Rockstuhl[2], Falk Lederer[2], Marius Peters[3], Lorenz Steidl[4], Rudolf Zentel[4], Seung-Mo Lee[5], Mato Knez[5], Andreas Lambertz[6], and Reinhard Carius[6]

[1] Institute of Physics, µMD group, Martin-Luther-University of Halle-Wittenberg, Heinrich-Damerow-Str. 4, 06120 Halle, Germany
[2] Institute of Condensed Matter Theory and Solid States Optics, Friedrich Schiller University Jena, 07743 Jena, Germany
[3] Freiburg Centre for Material Research, University of Freiburg, 79104 Freiburg, Germany
[4] Dept. of Chemistry, Pharmacy and Earth Science, Johannes Gutenberg University of Mainz, Duesbergweg 10–14, Germany
[5] Max Planck Institute of Microstructure Physics, Weinberg 2, 06120 Halle, Germany
[6] Institute of Energy Research, IEF-5 Photovoltaics, Forschungszentrum Jülich GmbH, 52425 Jülich, Germany

Received 5 July 2008, revised 22 September 2008, accepted 22 September 2008
Published online 18 November 2008

PACS 42.70.Qs, 78.66.Jg, 78.67.Bf, 81.07.Bc, 84.60.Jt

[*] Corresponding author: e-mail bilway@gmx.de

The concept of 3D photonic intermediate reflectors for micromorph silicon tandem solar cells has been investigated. In thin-film silicon tandem solar cells consisting of amorphous and microcrystalline silicon with two junctions of a-Si/µc-Si, efficiency enhancements can be achieved by increasing the current density in the a-Si top cell. It is one goal to provide an optimized current matching at high current densities. For an ideal photon-management between top and bottom cell, a spectrally selective intermediate reflective layer (IRL) is necessary, which is less dependent of the angle of incidence than state-of-the-art thickness dependent massive interlayers. The design, preparation and characterization of a 3D photonic thin-film filter device for this purpose has been pursued straight forward in simulation and experimental realization. The inverted opal is capable of providing a suitable optical band stop with high reflectance and the necessary long wavelength transmittance as well and provides further options for improved light trapping. We have determined numerically the relative efficiency enhancement of an a-Si/µc-Si tandem solar cell using a conductive 3D-photonic crystal. We have further fabricated such structures by ZnO-replication of polymeric opals using chemical vapour deposition and atomic layer deposition techniques and present the results of their characterization. Thin film photonic IRL have been prepared at the rear side of a-Si solar cells. Completed with a back contact, this is the first step to integrate this novel technology into an a-Si/µc-Si tandem solar cell process. The spectral response of the cell is presented and compared with reference cells.

1 Introduction Efficiency enhancement in photovoltaic cells is not only a matter of electronic properties, but also of various optical properties. Anti-reflection coatings (ARC) and grating couplers have been investigated [1–3], even water-repellant low-indexed ARC for module glass [4]. Also engineered light-trapping for solar cells has constantly been developed [5–7]. Several approaches have been exploring grating structures [8, 9] and light trapping structures [10], also for organic solar cells [11]. Also non-periodic backside reflectors from dielectric materials [12] show promising results, while combined approaches of front and backside improvement are being discussed as well [13]. The growing research field of photonics and photonic crystals [14] covers numerous approaches to improve solar cells [15, 16]. The optical design of solar cells and their components is therefore a major task in photovoltaic research already.

The parallel development of electronic and photonic properties and their interactions and possibilities of combined design is becoming an important issue. For an im-

provement of state-of-the-art 1st and 2nd generation PV cells and modules, even small improvements in efficiency on a technical level will contribute to the energy yield on short-term scale – but only if such advances can be introduced to established industrial fabrication lines with acceptable effort.

In recent years, the growing demand for solar energy – and thus efficiency and cost effectiveness – have lead to much interest in thin-film photovoltaic devices. The principle need for PV technologies with a short energy pay back time is obvious. Among the available technologies, the use of silicon as base material is of interest, because of its natural resources and the environmentally friendly chemistry of the material. Amorphous silicon thin-film technology has been offering very low cost per Watt peak in recent years, but unsatisfying efficiencies on standard conditions. The potential of the micromorph tandem cell will be discussed in the following.

1.1 Micromorph tandem solar cell The micromorph tandem cell consists of two different silicon junctions. The bottom junction (or cell) is made of microcrystalline Si (µc-Si) and about 1–2 microns in thickness. The top cell is of hydrogenated amorphous silicon type (a-Si:H), with a thickness of typically 0.2–0.3 microns. Both cells are thin-film devices, deposited from gas phase in PECVD or hot wire processes. Also, both are p–i–n devices, which in contrast to usual p–n devices use a built-in electric field to separate generated charge carriers. The cells are directly stacked on one another, with just a small tunnelling layer in between to avoid direct contact of n-type and p-type material from separate junctions. The cell is of so-called superstrate type: the process is top to bottom, starting with the a-Si cell on the front glass.

The combined thickness of such a tandem is about two microns, reducing price per watt peak, in terms of supply of resources and in terms of fabrication time. Both junctions are based on industrially available thin-film technologies and can cover large areas quickly: The deposition cycle of industrial modules can deliver one 1.4 m^2 module about every ten minutes. However, degradation of the top cell is an efficiency-limiting problem.

Figure 1 shows the schematic device. The front cell is deposited directly on a textured ZnO front glass, which serves as transparent front contact and superstrate. The etched texture is essential for light trapping in these cells. In between the junctions, doped tunneling layers terminate the n and p regions of the junctions against each other. The bottom cell follows conformally and is typically finalized with a (TCO connected) metal backside reflector and contact. The measured EQE of two junctions from the same tandem are shown in Fig. 2. High energy photons are being absorbed completely in the a-Si:H top cell, while red and infrared light is transmitted to the bottom cell, being absorbed by the µc-silicon. In the spectral range between 550 nm and 700 nm the top cell suffers from decreasing absorption coefficient of a-Si:H towards longer wavelengths. The spectral overlap of the EQE offers an opportunity to tailor the photon distribution between the two junctions by intermediate optical filters.

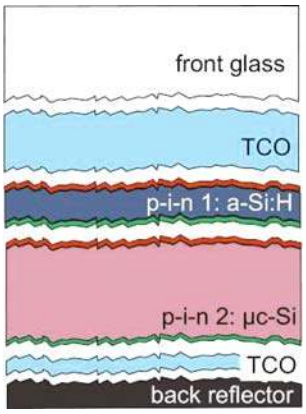

Figure 1 (online colour at: www.pss-a.com) Schematic of the micromorph tandem cell.

1.2 Potential Tandem cells are so-called 3rd generation PV technology. They fight fundamental losses in absorption and thermalization processes with the incorporation of more than a single electronic band gap within one PV device. Up to now, all top-rated high efficiency cells are III/V triple junction cells [17]. The combination of a-Si:H and µc-Si:H cells to build a tandem is motivated by the large difference in bandgap (~0.6 eV), as it contains the multi-junction advantage. The micromorph tandem features absorption edges of 1.1 eV (µc) and 1.7 eV (a). According to Green [18], the ideal edges of absorption for a series-connected two cell tandem for use in diffuse sunlight are 0.97 eV and 1.70 eV. The absorption edge of a-Si:H, however, is rather low at wavelengths above 550 nm, as Fig. 2 shows. Since both cells within the tan-

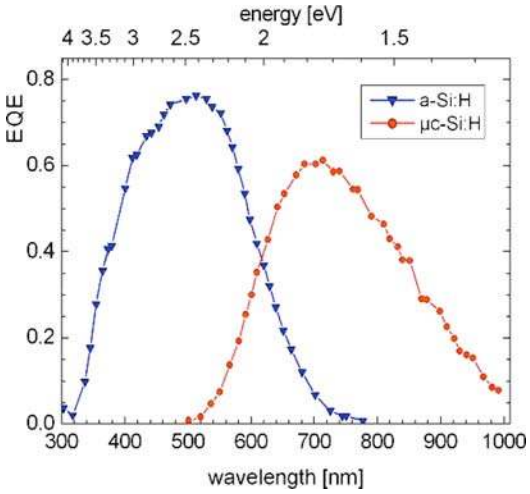

Figure 2 (online colour at: www.pss-a.com) Seperately measured external quantum efficiencies of the a-Si:H and µc-Si cells of one tandem cell. Their overlap is the spectral target area of photonmanagement.

dem divide the incoming photon flux from the sun among them, we have to consider the nature of this spectrum splitting.

Let us think of a theoretical tandem, consisting of two identical, lossless coupled, series-connected cells of the same electronic bandgap. Let us further say, that it shows the same efficiency as a (probably thicker) single junction of the same material, but as a tandem – delivering twice the voltage but half the current. If we now replace the top cell with a cell of higher bandgap, leaving everything else untouched, the voltage will increase. This is the impact of the multi-junction advantage on the absorption efficiency. Also, this leads to reduced thermalization, decreasing the losses to phonon excitation.

Due to its higher open circuit voltage V_{oc} the a-Si:H top cell delivers higher electrical power for each absorbed photon. So, in principle, the amorphous cell's absorption should be maximized. Optimization of the micromorph tandem cell will lead to a unique combination of 3rd generation potential with 2nd generation effectiveness in one low-cost & high efficiency thin-film solar cell.

1.3 Current matching Although maximization of absorbance by the a-Si:H cell is a key factor towards efficiency enhancement, further properties of the tandem have to be taken into account.

In order to eliminate losses from imperfect electrical conditions, the junctions of any series-connected tandem cell have to be current-matched. Uncompensated mismatch will prevent power from being delivered to the contacts as the smallest current will always dominate the tandem output. Micromorph tandems suffer from a current mismatch: the a-Si top-cell is limiting the electrical current of the whole tandem. Here the need for higher currents (and thus higher absorbance) in the top cell becomes obvious for a second cause. Table 1 shows the electrical properties of both junctions of a tandem in detail. The open circuit voltages (V_{oc}) as well as typical values at the maximum power point (MPP) in the tandem are shown. Typical short-ciruit currents are about 11 mA/cmm^2.

The currents differ about 10% which can partially be compensated by driving the a-Si cell not on MPP along the $j(V)$ curve, but at reduced voltage and increased current.

However, this is a trade-off, reducing efficiency at the electrical fill factor. A second solution: to increase the thickness of the top cell is not feasible either, due to the rather poor transport properties of amorphous silicon. Thickness is limited to few hundred nanometers in a-Si.

Repmann discussed the current matching at MPP [19], showing the initial and stabilized currents. The approach of optical current matching provides an additional way of in creasing the tandem efficiency there. In the ideal case, the solar spectrum can be spectrally splitted between the junctions after passing the top cell. A ratio of the high energy photons are then back reflected and absorbed in the top cell. If the optical current matching is optimized, both junctions could be driven at their individual MPP, which would lead to further enhancement of efficiency, since the top cell voltage could be increased again by several percent. Optical interlayers with appropriate filter properties are therefore investigated, both theoretically and experimentally with great effort.

Table 1 Voltages of the a-Si/µc-Si junctions.

	V_{oc} [V]	$V_{mpp,tan}$ [V]
a-Si:H	0.91	0.85
µc-Si	0.50	0.35

2.1 IRL state of the art The basic function of any intermediate reflective layer (IRL) in a tandem cell is the back reflection of a certain ratio of incident photons that have not been absorbed in the top cell. The exact measure of this ratio is defined by the actual current mismatch that has to be compensated.

The problem of current mismatch and the concept of the intermediate reflective layer for silicon tandems have been investigated in many ways in the last decade. The micromorph tandem was a topic at Forschungszentrum Jülich, Germany [19–21], University of Neuchâtel, Switzerland [22–24] and Kaneka corporation, Japan [25]. Also micromorph cells on flexible plastic substrates have been reported, e.g. by Haug et al. [26], with incorporated IRL of a silicon oxide compound. They achieved current matching up to 0.2 mA/cm^2 of remaining mismatch at tandem currents of j_{sc} = 11.2 mA/cm^2. The common approach to all reported work is the use of a massive TCO layer. It leads to reflection at the interface between top cell and IRL, as well as between IRL and bottom cell. This reflectance is mainly described by Fresnel's equations and strongly depends on the thickness of the interlayer. The use of a finely tuned spectrally narrow thin-film oscillation leads to significant angular dependence of the interlayer spectrum splitting efficiency. Nevertheless, the massive IRL is a very attractive concept, because of its high compatibility with available deposition technologies. Also remarkable enhancements have been achieved: Kaneka reported initial efficiencies of 13.4% in a small module and 15.0% for a lab cell of 1 cm^2, compared with 11.7% listed in the 2007 solar efficiency tables [17].

Investigations of such layers by Krc et al. in 2006 revealed: "Optical analysis of the interlayer revealed possibilities for significant improvements of $J_{SC,top}$ (>25%) or thickness reductions $\Delta d_{i,top}$ (>50%) for interlayers with small refractive index (n_{inter} < 2.0)" [27].

Their results included also the observation that using massive interlayers, strong enhancements of the absorption (red/NIR) in the top cell will significantly reduce bottom cell illumination even at optimized thicknesses. This is caused by the spectrally wide overall reflectance at the interfaces, leading to unwanted back-reflection losses also in the long-wavelength regime. Low refractive index of the IRL is in any case favoured, as low as even n_{IRL} = 1.2.

An optically optimized tandem cell would be composed from a highly efficient light trapping front, a very thin a-Si layer that is possible because of an intermediate reflective layer (IRL) and a thin but efficient µc-Si layer, allowed by the good light trapping and a diffuse back side reflector.

2.2 Requirements The requirements for any simple and also for any sophisticated intermediate filter can easily be deducted from already discussed properties. It should provide the following three conditions:

– First, the IRL should deliver a spectrally limited back-reflectance for the a-Si top cell where the EQE of both junctions is defining our spectral region of interest.

– Second, the IRL should to be transparent for red and infrared light.

– Third, the IRL must exhibit a sufficient electrical conductivity, as the micromorph tandem is a series-connected 2-terminal device.

The quantification of these requirements is somewhat fuzzy since there is no standard micromorph tandem cell. Also can the thickness of both junctions be used within certain limits to tune absorbance to match the tandem to a promising photon management provided by an IRL.

However, the reflectance has to modify the spectral photon distribution in order to achieve current matching of a certain tandem cell. The mismatch is typically in order of magnitude of 10%. Red transmittance has to be as high as possible and the resistance of the integrated IRL should be clearly below ~2 Ω to keep the voltage drop within the critical limits of the cell's diode characteristic.

3.1 IRL design Between different possible IRL designs to improve a-Si absorbance, we can distinguish between simple (massive) IRL and 1D, 2D and 3D structured IRL, belonging to the material class of photonic crystals (PhC). Homogeneous IRL introduce a Fresnel type reflectivity. Befittingly tailored thickness of the interlayer produces one thin-film oscillation in the spectral region of low absorption. Despite their denomination as homogeneous in this article, these layers may also be porous on the micro or nano scale but always act as one single optical layer of effective refractive index n_{eff}. One dimensionally periodic IRL, so-called Bragg stacks, feature a spectrally limited band stop reflectivity. 2D periodic structures do not posess this band stop property, besides possible thin-film effects, but produce diffraction patterns according to their lattice constant and type of lattice. They can be prepared with lower refractive index, if the periodicity is fabricated with 'air' holes. 3D PhC finally have the potential to combine all mentioned effects in one photonic device. They may also possess very low effective indices, even less than typical 2D structures due to their volume filling fractions. They develop a strong stop band reflectivity between lattice planes (Bragg reflection) and add diffractive properties from their 2D surfaces and a variety of lattice planes or, as denoted in terms of photonics, higher band features. The incorporation of an internal reflector is preferably realized as a real intermediate layer, placed in between the two junctions and therefore consisting of transparent conductive oxides – 2D or 3D structuring of one of the silicon interfaces will lead to strongly increased recombination rates. Preferably, any IRL should be feasible as add-on to already established fabrication processes, leaving both cell depositions unchanged.

After massive IRL have already proven enhancement potential experimentally, and with 2D gratings being discussed in a variety of functions, a novel approach to IRL designs is the use of 3D photonic crystals (PhC): the design of an interlayer of periodically structured refractive index in all three dimensions.

The potential of different IRL approaches towards current enhancement in the top cell have been investigated for massive layers, Bragg stacks (1D) and inverted opal PhC (3D). High reflectivities with a spectral width smaller or as wide as the overlap of the EQE should be targeted.

3.2 Concept: inverted opal IRL An internal reflector has to be compatible with the random roughness of state of the art thin–film cells, or it should introduce strong diffractive effects itself, justifying a planarization of the a-Si backside.

Dependent of the lattice constant (sphere diameter), 3D PhC will show strong diffractive properties. The onset of diffraction at the interface between silicon and the PhC is given by Eq. (1):

$$\frac{\omega a}{2\pi c} \geq \frac{n_{\mathrm{PhC}}}{n_{\mathrm{Si}}} \approx 0.3\,. \tag{1}$$

The diffraction limit is also shown in Fig. 3. The photonic properties of inverted opals can be deducted from the photonic band structure (BS), shown in Fig. 3. Photonic bands are summarized solutions to the photonic master

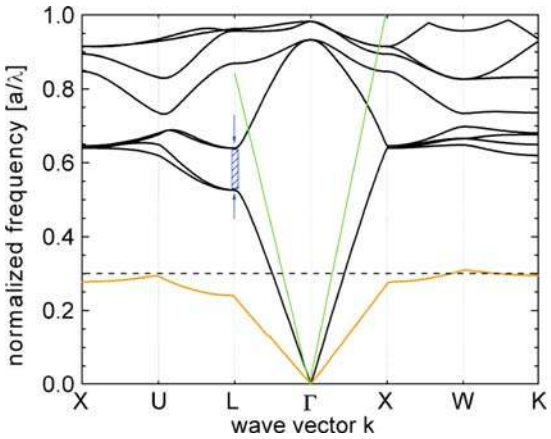

Figure 3 (online colour at: www.pss-a.com) Photonic bandstructure (BS) of inverted opal of dielectric contrast 1.00/6.25 (air/indium-tin oxide). In ΓL-direction, a stop gap opens up at $0.58\alpha/\lambda$ (arrow marks). The onset of diffraction is inserted at about $0.3\alpha/\lambda$ [28].

equations and show the allowed frequencies for modes of certain $\boldsymbol{k}$-vectors. The BS yields for perfect and infinite PhC. Eigenfrequency calculations have been performed with MPB [24]. The stop gap in ΓL-direction leads to back reflection of incident light in this direction, if the normalized frequency lies within the gap. The optical modes can not propagate in the gap: they will be reflected. The key parameter to strong photonic effects is the refractive index contrast or the ratio of permittivities. A slope of the bands indicates a spectral shift, if the direction of incidence is changed. The spectral position of their centre frequency however, is affected by the lattice constant $a = \sqrt{2} \cdot d$.

This is expressed by a spectrally limited reflectance of the PhC, its width related to the gap in the photonic BS.

There are two effects combined in the 3D PhC, the selective specular (photonic) reflectance and the diffraction grating. According to Bragg's law, the spectral position of the reflection (Bragg peak) from interference of ⟨111⟩ lattice planes of a colloidal photonic crystal follows Eq. (2):

$$\lambda_{(111)} = 2\left(\tfrac{2}{3}\right)^{1/2} d \cdot \left(n_{\text{fit}}^2 - \cos^2 \Theta\right)^{1/2}, \qquad (2)$$

where d is the diameter of the spheres, n_{fit} is an effective refractive index, and Θ is the angle of incidence against the ⟨111⟩ plane. This effective index however, is defined within the photonic stop gap. It is not equal to, but mostly in order of magnitude of the effective refractive index in long wavelength limit, which is why we address this index as a fit parameter. The reflectance wavelength of opaline films as well as their replica depends on the refractive index contrast between spheres and the so-called host and the lattice constant of their periodic nano-structure. Highly indexed host materials surrounding hollow (air) spheres lead to stronger photonic properties than low-index materials with the same lattice parameters.

In this paper, we focus on the photonic stop gap, which depends on the lattice constant of the PhC. Also we discuss the influence of diffractive properties at the chosen crystal parameters in efficiency enhancement.

3.3 Simulation of optical properties The optical properties of finite and thin films of (inverted) opaline photonic crystals and the influence of interfaces have to be investigated with other numerical methods.

We used the scattering matrix method (SMM) as proposed by Whittaker and Culshaw [29] for the calculation of the coefficients of reflection and transmission. The PhC structure is therefore implemented as a 3D unit cell infinitely reproduced within the x,y-plane and divided in layers, so-called chunks, like the one sketched in Fig. 4, along the vertical z-axis.

This method is extremely fast compared with rigorous methods, as is approximates the correct solution of the fields. Only with an infinite number of Fourier orders solved, the correct solution is obtained.

Therefore, all the calculations concerning efficiency impact of the IRL have been performed with rigorous Fourier methods, especially the layered Korringa–Kohn–Rostocker method (KKR). It uses an expansion of the fields to spherical waves in surrounding geometries of spherical symmetry, which makes it very well suited for all opaline PhC.

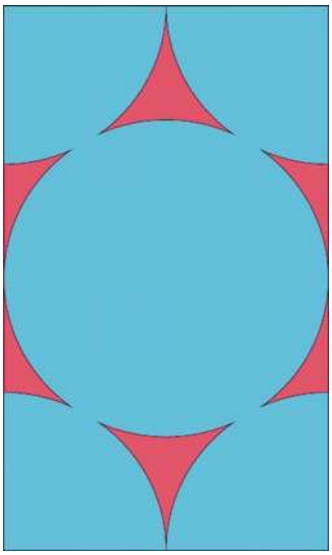

Figure 4 (online colour at: www.pss-a.com) 2D chunk of the fcc unit cell for SMM.

Reflectance spectra obtained via SMM are plotted in Fig. 5. Here, the three stages of the fabrication process are resolved: opal template, infiltrated composite and inverted opal. These processes are discussed in detail in Section 5. The SMM results show, that compared with the typical opal reflectance, the inverted structure provides a larger spectral width and a significantly higher reflectance, which is caused by the higher index contrast. Spectra of (inverted) opals show only small deviations for different polarizations. The composite structure shows nearly no polarization dependence at all. Based on these calculations,

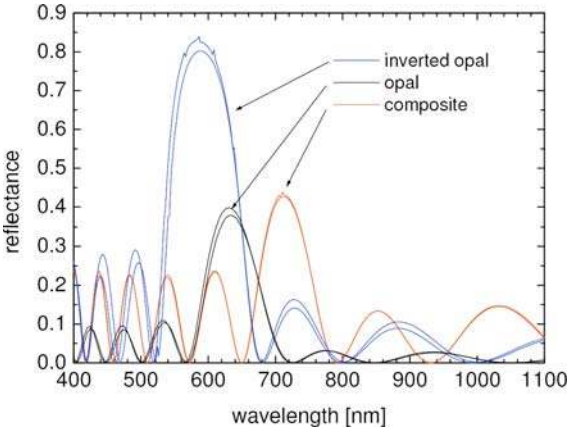

Figure 5 (online colour at: www.pss-a.com) Calculated reflectance spectra from scattering matrix simulations of 1.00/2.89 inverted opal, composite and opal template (6 layers, each) with d = 300 nm [30].

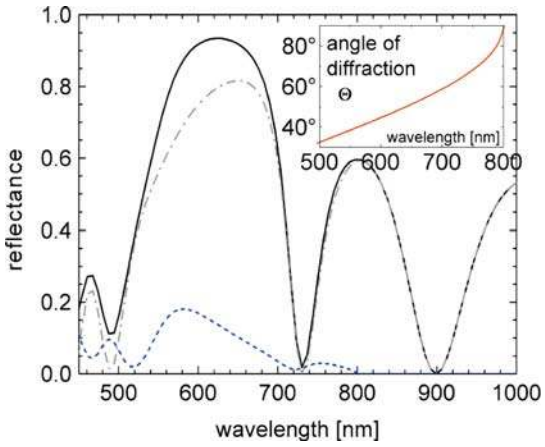

Figure 6 (online colour at: www.pss-a.com) Calculated reflectance spectrum from KKR simlulation of 1.00/6.25 inverted opal (6 layers) with $d = 250$ nm air spheres. Zero (dot, dash) and first orders (short dash) are plotted separately, the inset shows sufficiently high diffraction angles as a function of wavelength [28].

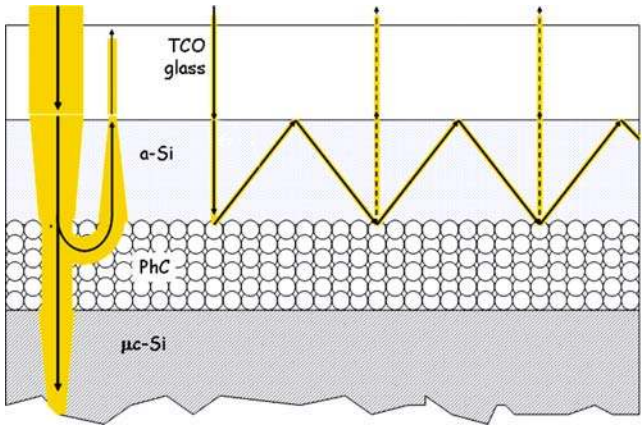

Figure 7 (online colour at: www.pss-a.com) Schematic optical path inside the top cell for specular zero order reflectance (left) and diffracted higher orders (right). The calculation for planar silicon layers leads to trapping of diffracted light within th a-Si layer and to strongly enhanced absorption of the small diffracted ratio light [28].

we are able to follow the experimental progress of sample preparation by means of optical spectroscopy.

The results from KKR simulations are shown in Fig. 6. The reflectance of zero diffraction order (specular) reflectivity and first orders are plotted. Also the diffraction angle is shown in the inset for first orders. Analogous to the SMM model, the structure for KKR method was implemented as a 6 layer thin film of perfect fcc inverted opal lattice. In contrast however, we used a higher contrast in the permittivity 1.00/6.25 to estimate realistic limits of the photonic properties. The results show a spectrally limited but rather wide reflectance peak centered at about 620 nm. The FWHM is about 170 nm, the base width between the minima is 230 nm. Reflectance reaches 93%. From planar interfaces and perfectly coherent excitation, strongly pronounced Fabry–Perot oscillations (FPO) arise. They are higher in amplitude than in the presented SMM spectra, because of the difference in dielectric contrast $\Delta\varepsilon$. The first order back diffraction into the front half space is comparably weak but experiences large deviations from snell's law. The diffractions angles are always larger than 30°. Absorption is neglected, termination of the PhC is defined by half spaces assumed as silicon, approximating surroundings of the silicon tandem cell.

4 Top cell enhancement calculation To estimate the influence of an inverted opal IRL at the back of an amorphous silicon top cell, we use the results from our KKR simulations. Focus is on the absorption of light within a-Si in the spectral region of its low absorbance between 550 nm and 750 nm. The thickness of the a-Si:H junction is D. The absorbance A_S in the top cell is increased by photonic back reflection in zero order A_0 and higher order diffraction A_{1+} because of the reflectances R_0 and R_{1+} respectively. The standard absorbance of the top cell is simply defined as in Eq. (3):

$$A = 1 - T_S = 1 - \exp(-\alpha D). \tag{3}$$

Using the transmittance T_S through the top cell.

For zero order an optical path of D after back reflection is assumed. Not absorbed reflected intensity is lost. For back diffracted light, a path increase according to the diffraction angle Θ has been calculated according to Eq. (4).

$$A_{1+} = 1 - \sum_{m=0}^{\infty} (1 - R_{1+}(\lambda))^m \cdot \exp\left(-m\frac{2\alpha D}{\cos\Theta}\right). \tag{4}$$

Total internal reflection (TIR) at the front of the a-Si top cell was assumed for the received angles, m is the number of these reflections. Thus, the dominant loss mechanism becomes back diffraction by the PhC itself, coupling the

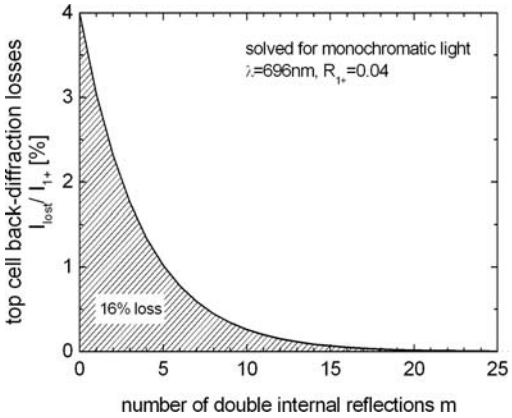

Figure 8 Calculated intensity loss in the a-Si top cell, caused by back diffraction of light. About 84% of diffracted intensity (of 4%) can be trapped in the top cell, 16% of it are lost via reciprocity of the PhC diffraction.

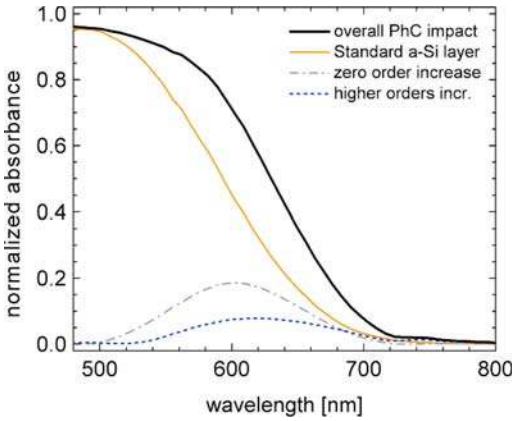

Figure 9 (online colour at: www.pss-a.com) Absorbance enhancement by a 6 layer inverted opal of 1.00/6.25 permittivity contrast. The sensitivity of the cell is extended towards the red part of the spectrum by direct and diffractive back reflection of light. The impact of higher orders is remarkably high although their reflectance is of poor magnitude [28].

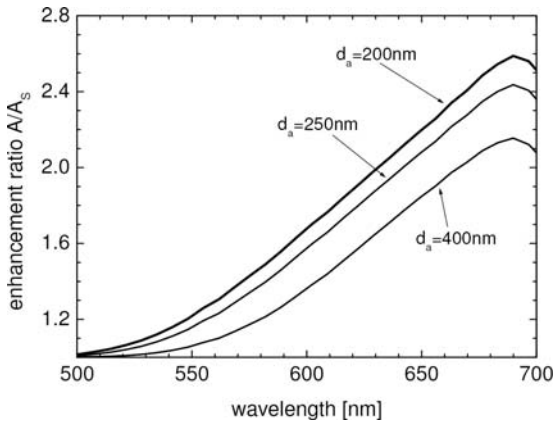

Figure 10 Absorbance enhancement ratio for different thicknesses of the a-Si absorber layer: The impact of a matched photonic IRL increases with thinner top cells.

first orders back into zero order after TIR.

$$A = A_S + A_0 + A_{1+} = 1 - T_S + T_S R_0 (1 - T_S) + T_S + T_S R_{1+} A_{1+} . \quad (5)$$

This is sketched in Fig. 7. Although the reflectance into higher orders is rather weak, the light trapping can lead to significantly enhanced absorbance of the diffracted intensity. A monochromatic solution of Eq. (5) is shown in Fig. 8, where the remaining intensity within the a-Si cell has been solved.

Light of 696 nm wavelength experiences only about 4% of diffraction, but 84% of this small ratio are being captured by the top cell after being trapped in total reflection. The shape of the curve in Fig. 8 results from back diffraction losses caused by the PhC itself, smoothed by continuous absorption in the cell. The effect of this enhancement on the absorbance of a standard amorphous silicon thin-film cell is shown in Fig. 9. Here, the impact of the discussed optical properties is obvious. The spectral position of the reflectance, both – direct and diffractive – is well placed in the spectral region of low absorption of a-Si. As a result, the back reflection enhances absorbance in the top cell there, which leads to a red-shift of the absorption function. The a-Si cell sensitivity has been extended towards the red.

The thinner the a-Si top cell is, the less absorption it can provide. Since thinner cells have less transport problems, the effect of our IRL concept on different thicknesses of the top cell is of interest. Figure 10 shows three different thicknesses and the expected enhancement ratio of our model. In thinner cells, the ratio of diffracted and specularly reflected light on the enhacement is changed.

Thinner cells still benefit from the path increase of diffraction, but have reduced increases from direct reflection. Since they have only reduced absorbance anyway, more light hits the interlayer and is therefore back reflected by the IRL, which pushes the device's importance in this case. The combination of thinner top cells and matched intermediate reflector is therefore considered a feasible and tempting approach.

5 Experimental realization The preparation of inverted opals is a multi step process. After substrate preparation, an opal template is produced as a thin film on glass or the back side of amorphous silicon. It is then tempered. Afterwards, the template is infiltrated with a transparent conductive oxide (TCO), in our case zinc oxide (ZnO). This step is referred to as replication, since it is the formation of a structural negative of the template. Third and finally, the template is destroyed chemically or via calcination in a furnace, leaving the desired inverted opal film. We discuss the first and second steps in more detail, as they are of importance for the technological aspects. The

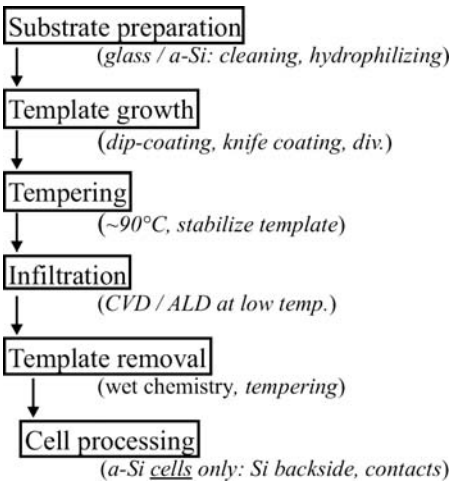

Process sequence: the different steps of sample processing, starting with bare microslide glass or a-Si solar cells to finalized PhC filters at their back sides or contacted solar cell prototypes.

process of sample preparation is summarized in the overview scheme below.

The synthesis of the monodisperse PMMA colloids were done by surfactant free emulsion polymerization [31] and crystallized into opaline films using vertical [32] and horizontal crystallization approaches [33] as well as spray induced self-assembly [34]. Airbrush experiments were performed with a commercially available apparatus from Sil.Air. For the horizontal crystallization coating-knifes and a lab-made doctor blade apparatus were used as well as several experimental knife coating devices.

We choose chemical vapour deposition (CVD) and atomic layer deposition (ALD) methods for the purpose of infiltration with transparent conductive oxides. In both cases the opaline film is exposed alternatively to gaseous precursors, either $Zn(Me)_2$ (DMZ) or $Zn(Et)_2$ (DEZ) as first and H_2O as second one. The two reagents adsorb to the surface of the colloids and react there to ZnO. If after every precursor deposition, the remaining gaseous chemicals are flushed out of the reaction chamber, the surface reaction becomes completely self-terminating.

Replication via chemical vapour deposition (CVD) following a literature procedure [35]. A solution of dimethyl zinc in toluene CDMZ, 2M, Aldrich) respectively deionized water from a Milli-Q-system (Millipore), which were kept in separate glass flasks, were used as precursors. Nitrogen was bubbled through the solutions at a rate of ~200 ml/min alternatively to blow the precursor into the reaction chamber with the opal sample, which was kept at 90 °C. After each cycle a nitrogen purge was applied to remove excess material. A typical run appears as follows: 4 minutes water purge, 4 minutes pause, 90 seconds DMZ purge, 3 minutes pause, 3 minutes nitrogen purge. Purge times and cycle number were varied. A sufficient filling was observed after 5–7 cycles, when the optical appearance of the opal changed and the bragg-reflectance vanished due to refractive index matching. This was verified using UV–VIS optical measurements. Replication via atomic layer deposition (ALD) was performed in a commercially available Cambridge Nanotech, Model Savannah.

For ALD process, pure undiluted DEZ precursor from Sigma-Aldrich has been used as delivered. The temperature of the sample during reaction was kept as low as 60 °C. The details of the deposition cycles are shown in Table 2.

Since the resulting deposition is conformal, the desired deposition thickness defines the number of cycles to use.

Table 2 Deposition cylce of ALD.

	material	pulse [s]	exposure [s]	N_2 purge [s]
precursor A	$Zn(Et)_2$	0.1	5	10
precursor B	H_2O	1.5	15	150

pulse: duration of precursor influx, exposure: allowed reaction time, purge: duration of nitrogen flushing; at substrate temperature of $T = 60$ °C. The low temperature makes long purge times for water necessary.

We choose 40 nm of coating thickness. While about 23 nm are the limit for conformal infiltration with $d = 300$ nm spheres, a little additional thickness on the outer surfaces and on top of the PhC film provides improved mechanical stability and easier electrical contact procedures later on.

5.1 Template preparation Artificial opals from monodisperse polymer or SiO_2 colloids are commonly used for the preparation of templates for inverted structures (opal replica). They are crystallized into the cubic densest packing and removed after the filling of the interstitials leaving behind the opal replica.

It is thus necessary to start with colloids, where this size can easily be adjusted to obtain a replica with the desired selective reflection. In addition it must be feasible to remove the colloids after replica formation without damaging the final photonic structure.

Therefore, we choose poly-methyl-metacrylat (PMMA) spheres for opal template preparation. This polymer can be removed under mild conditions using organic solvents or oxygen plasma [33, 36] without affecting the inverted structure or the Si-layers. Also, the PMMA spheres can be prepared by surfactant free emulsion polymerization (SFEP) whereby the size of the resulting beads is controlled by the monomer to water ratio at a given reaction temperature and initiator concentration. In Fig. 11 the relationship between the monomer concentration and the size of the colloids is shown. An analytic evaluation of these data allows the prediction of the colloid size within 20 nm using the following equation [31, 37]

$$\log d = 1/3 \log [M] + 2.471 , \tag{6}$$

where d is the colloid diameter (in nm) and M is the monomer concentration (mol/l). Monodisperse colloids between 200 nm and 500 nm in size can be produced.

Opaline films prepared from these spheres exhibit Bragg peaks between 400 nm and 1000 nm, as shown in Fig. 12.

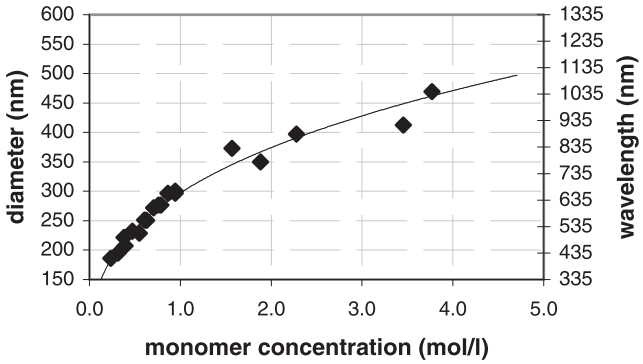

Figure 11 Dependence of the sphere diameter on the initial monomer to water ratio for PMMA at an initiator concentration (potassium peroxodisulfate) of 12 mmol/l. The correlation between the bead diameter and the Bragg-reflectance of the corresponding opal is also shown.

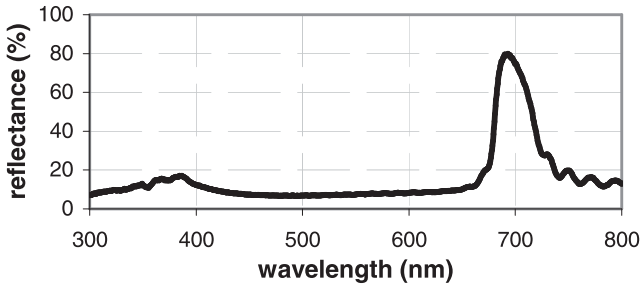

Figure 12 Reflection spectrum of an opal of in average 47 monolayers of PMMA spheres (bead diameter: ~312 nm); bandwidth $\Delta\omega_{gap}/\omega_{gap} = 0.052$.

Thus, the selective wavelength of the replica can be adjusted easily to values from 550 nm to 680 nm, which are needed for the intended application for the micromorph tandem cell. The photonic properties of this replica depend on the in-filled material and achievable filling fractions (see Section 3). The optical properties can be altered also via post-processing (e.g. tempering) of the infiltrated material. Sphere sizes of 284 nm and 294 nm (Bragg-reflectance at 630 nm and 654 nm, respectively) have been used for several template experiments. Also 360 nm spheres have been used for prototyping experiment in Section 7.

Different crystallization methods were applied to prepare opaline films from the PMMA spheres. The aim of these experiments was twofold. First, thin opaline films with high quality (strong reflectance and narrow bandwidth) should be prepared and secondly, an approach should be used, with which a large area can be covered with an opaline film. Examples are shown in Fig. 13.

With a vertical crystallization method we achieved thin and homogeneous films with controlled thickness [16] as shown in Fig. 14. For this approach the substrate was drawn vertically out of a suspension of colloids in water with a speed of several 100 nm/s, whereas crystallization takes place in a moving meniscus. However, a decrease in film thickness goes along with a lowering of the reflectance intensity. Also the bandwidth of the Bragg-peak is broadened distinctly below a monolayer number of 15, which is close to the critical thickness for a narrow bandwidth reported in [38].

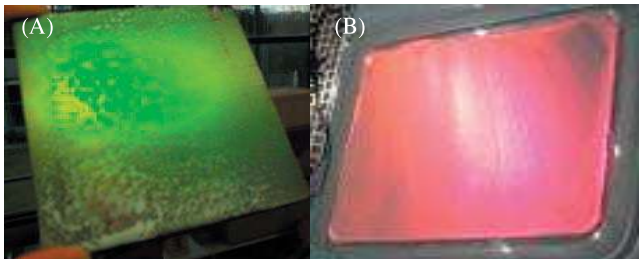

Figure 13 (online colour at: www.pss-a.com) Examples of large-scale opaline films. (A) opal on a glass substrate (10 × 10 cm) prepared by spraying, (B) horizontally dried opal film (40 × 25 cm).

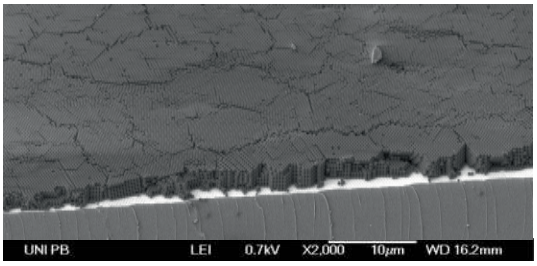

Figure 14 SEM micrograph of a thin opal template on silicon with constant thickness; A. Redler and P.-T. Miclea.

Although the crystallization in a vertical meniscus provides good results, this approach is time-consuming and limited to smaller substrates. Larger opal films can be prepared by horizontal crystallization. Here the thickness of the film can be adjusted by the amount and the concentration of the suspension which is dried on a given substrate area. E.g. with a coating knife (doctor blading) it is possible to prepare large scale opaline films of good optical quality and homogeneous thickness. Opaline films of about 50 monolayer in thickness prepared by this method exhibit a reflectance close to 80% and a narrow bandwidth ($\Delta\lambda/\lambda$) of about 5% (see Fig. 12).

The usage of a spraying apparatus is also a promising method for the covering of large areas with an opaline structure. For this purpose, suspensions of high concentration were sprayed directly on the substrate using airbrush equipment. Opal films are built after a few minutes of drying [34]. Figure 13(A) shows an opal film of 100 cm^2 produced with this approach.

Since there are few experimental limitations for the area size on which the colloidal suspension is spread, substrates of almost any size can be covered with a colloidal film. As example a PMMA opal of 1000 cm^2 size – prepared in this way – is shown in Fig. 13 (B).

Thus the first goal to prepare large opaline films as templates for the inorganic replica can be reached. Preferably, the templates are tempered at about 90 °C for a few minutes to strengthen the interconnects between the so far singular hard spheres. This improves mechanical stability and leads to the so-called tubes, small PMMA extensions between the nano spheres. The next steps are the infilling and replication of the PMMA opals.

5.2 Inversion As a conductive replica is desired, it is the first step to fill the opaline voids with ZnO, using vapour deposition methods. This deposition is conformal, which is setting limits to the possible filling fractions. Instead of a complete inversion, conformally inverted opals can be fabricated with up to 22.3% of volume filling (here the TCO), instead of 26% in theoretical replication. After infilling, the PMMA-templates were dissolved in THF and the ZnO replica were obtained. Figures 15 and 16 show SEM images of ZnO-replica prepared with CVD. The in-depth infiltration of the template succeeds very well, as the vaporous precursors fill even narrow spaces. On top of an

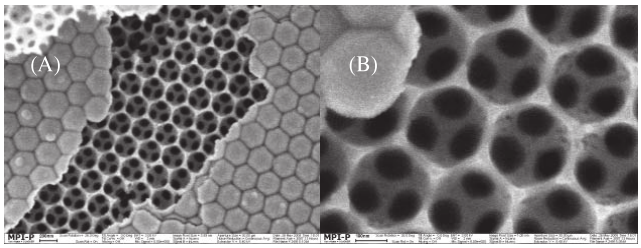

Figure 15 SEM micrographs of a ZnO-replica prepared with CVD from 292 nm PMMA sphere opal. (A) Partially uncovered surface. (B) Magnification showing the ~290 nm air holes and the ~25 nm ZnO framework thickness.

inverted sample – or rather at all outer surfaces, there is still the appearance of the original opal template, because of the conformal replication. At least unless the surface is opened, as shown in Figs. 15(A) and 17(A). It is important that during this process cracking-voids in the primary opaline film fill-up from bottom to top with ZnO (see Fig. 16). This is highly desirable as the primary cracks are thus transformed into an electrically conductive micro-grid that connects top and bottom cell.

Examples of ALD processed thin-film samples are shown in Fig. 17.

6 Characterization Structural characterization has been performed with SEM, as already shown in Section 5. The three key properties are two of optical kind: reflection and transmission and the electrical conductivity. The results on transmission will be presented with the aspects of integration in Section 7.

6.1 Optical properties To verify the results obtained from SMM calculations, we measured reflectance of opal templates, composite samples and inverted ones. Under an optical microscope of type Olympus BX51, the last process step of template removal looks as shown in the two photographs of Fig. 18. The spectra of all three sample types are shown in Fig. 19. They have been measured with a lab-built spectrometer setup, using a monochromator of type

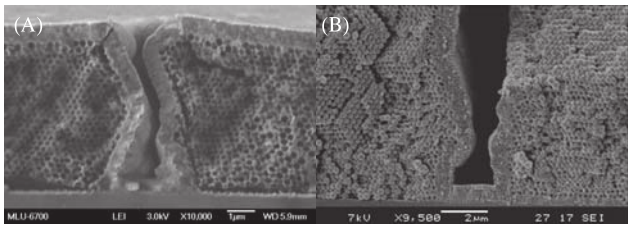

Figure 16 SEM micrographs of CVD processed inverted sample: the view on cleaved edges presents the CVD deposition down an opaline drying crack on two thick samples. This surplus ZnO coating is deposited from top to bottom of the photonic IRL and can form a electrically conductive micro grid to connect top and bottom cell: (A) inverted sample with surplus deposition; (B) composite sample with massive surface deposition, also down to the substrate.

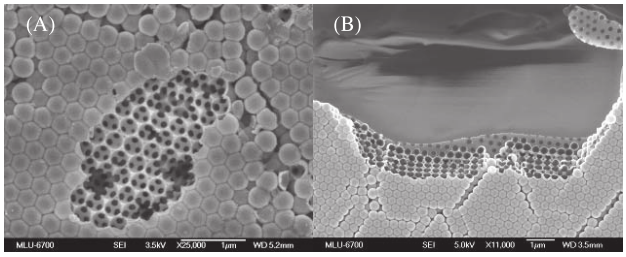

Figure 17 SEM micrographs of ALD processed inverted samples: opened surface of the confomal coating shows 3D PhC structure (A). Cleaved edges give insight into film thickness and crystalline quality (B). Here, the octahedral voids are visible at a cut perpendicular to crystallographic X-direction.

HB550i by Jobin–Yvon and a 250 W halogen light source. Reflectance was measured at 10° angle of incidence.

The predicted behaviour has been verified for all three process steps. The significant reflectance increase of the inverted sample dominates the optical properties in comparison.

The angular dependence of the reflection peak can be measured in a 2Θ setup for the angle of incidence, keeping the angle adjusted for specular reflection. With increasing angle, the peak is blue-shifted, which is shown in Fig. 20. This can also be foreseen from the photonic band structure. There the bands below and above the stop gap bend towards higher frequencies when the angle turns away from incidence along ΓL-direction. The angular shift however, is clearly pronounced, but falls below half the normal amplitude not until reaching 45°. Remarkable in all reflectance spectra of inverted samples is, that the FPO are much wider than in opal or composite states of the sample. This is an attribute of the very low effective index of the inverted opals.

6.2 Electrical properties In order to measure conductivity or resistivity, samples have been contacted on top with interdigitated contact fingers. The fingers have been sputtered with gold directly on the ZnO surface. The obtained $I(V)$ data from source meter measurements are shown in Fig. 21. The contact line of this sample measures

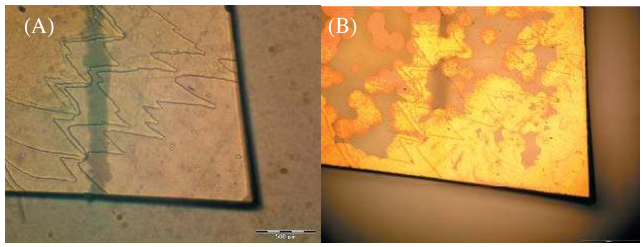

Figure 18 (online colour at: www.pss-a.com) Reflectance microscopy photographs (A: $M = 20$, B: $M = 10$) of the same sample before and during template removal. The golden impression develops after removal of the PMMA spheres and verifies the final inversion process step.

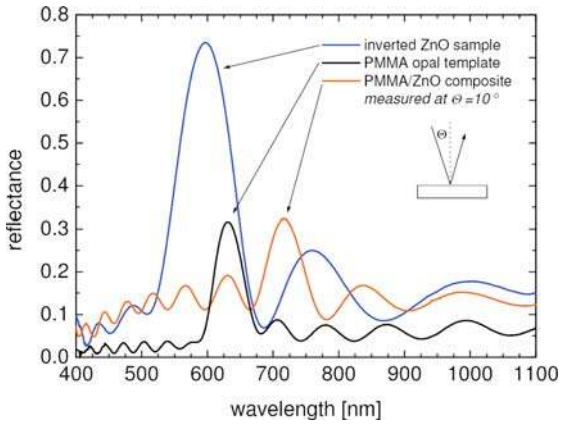

Figure 19 (online colour at: www.pss-a.com) Reflectance measurements of samples from all three process steps: the predictions from prior SMM simulations (Fig. 5) are in good agreement [30].

25 mm in length across the sample. The thickness is 2 µm, the distance between the gold contacts is 1 mm. The contacts themselves show resistances of few ohms per centimeter and do not offset the results.

The obtained value of $R = 198$ kΩ of resistance leads to a resistivity of $R_s = 10\ \Omega\ \mu m$ for bulk conduction through the whole sample. In case that only the uppermost ZnO layer on top of the sample carried the current in these measurements, the resistivity would be normalized by the 40 nm of this thickness, leading to $R_s = 0.2\ \Omega\ \mu m$. For an IRL of 1.5 µm thickness (6 layers at $d = 300$ nm), the resistance can therefore be estimated to measure between 0.3 Ω and 15 Ω. For the micromorph tandem cell, a resistance of 2 Ω has to be considered critical. The measured conductivity of the undoped ZnO from ALD processing is close to the required order of magnitude, but still requires improvement. Any advance in terms of conductivity will reduce the electrical losses of the common current in the series-connection between the two junctions.

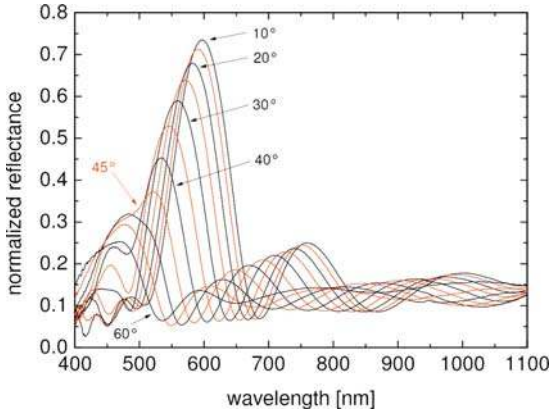

Figure 20 (online colour at: www.pss-a.com) Angular spectroscopy, performed on a thin-film ZnO inverted opal on glass. The angle of incidence has been changed from 10° to 55°. The amplitudes have not been cosine corrected for better survey [30].

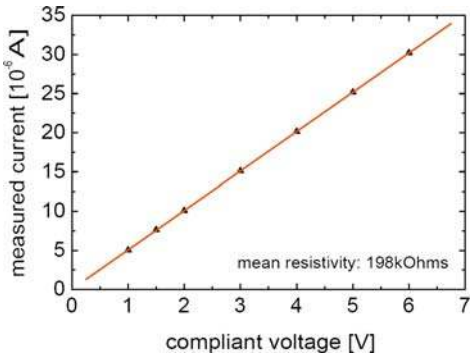

Figure 21 (online colour at: www.pss-a.com) $I(V)$ curve, measured at room temperature with a Keithley 2400 sourcemeter. The resistance is constant, its value 198 kΩ.

Additionally to measurements of current and voltage, electro chemical impedance spectroscopy (EIS) has been performed on the same sample. EIS gives access on the impedance over a wide frequency range and also resolves the phase shift of a sample on the offered AC modulation. A constant impedance in the EIS spectrum reveals ohmic resistance, while a linear increase with decreasing frequency is typically linked to capacitive dielectric behaviour. The results of our measurement are shown in Fig. 22 and reveal a constant ohmic character of impedance up to frequencies of kHz range. In conclusion, only the value of resistivity has to be decreased, the material is suited as processed.

7 Integration All investigations on samples in free space, i.e. not in or on a silicon solar cell, did show the desired properties in all steps of our work. However, to verify the potential of an application, we investigated three additional aspects. The transmission onto a half space silicon solar cell is one of the critical requirements and will be presented first. The integration into a solar cell process of the a-Si µc-Si tandem cell was studied in a prototyping approach, in order to verify the compatibility of the so far

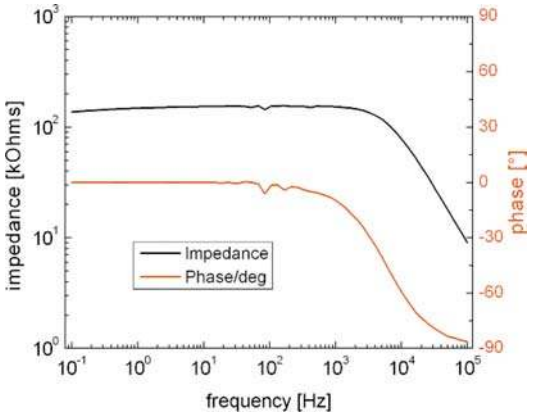

Figure 22 (online colour at: www.pss-a.com) Electrical impedance spectrum of inv. opal thin-film sample: The PhC behaves clearly ohmic up to kHz frequency range.

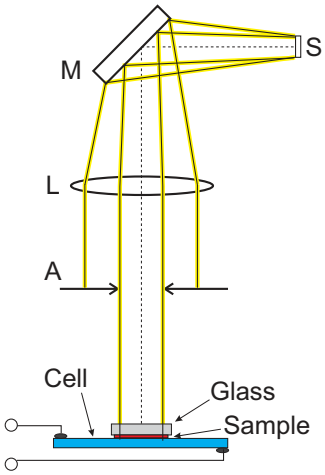

Figure 23 (online colour at: www.pss-a.com) Schematic setup for the integrated cell transmission measurement [30].

completely separate processes. Also, a combination of a typical random rough superstrate top cell with the self-organizational growth of our opal templates has been explored.

7.1 Integrated transmission To obtain experimental data on the transmittance of the fabricated IRL on the µc-Si bottom cell, an integrated setup has been built. Instead of a microcrystalline cell, a commercial silicon (mono crystalline) mini cell has been used. This cell works as a detector in the spectroscopic setup (Fig. 23). The illumination from a halogen light source takes place behind the monochromator slit (S). Mirror (M) and lens (L) collimate the light, while an aperture (A) reduces the spot size to the size of the sample.

The spectral answer of the cell defines only the transfer function of the setup: as reference data we use the transmit-tance $T_{\mathrm{int},0}$ of a cleaned and unprocessed sub-strate glass that is placed directly on the solar cell. The actual measurement of $T_{\mathrm{int,ZnO}}$ of a ZnO inverted opal film on substrate glass of same type is normalized with this reference by division of $T_{\mathrm{int,ZnO}}/T_{\mathrm{int},0}$. The IRL sample is placed upside down, with the PhC in contact with the solar cell and the glass substrate facing the incident light. The glass is 1 mm thick, the IRL itself measures about two microns in thickness. The resulting spectrum is shown in Fig. 24.

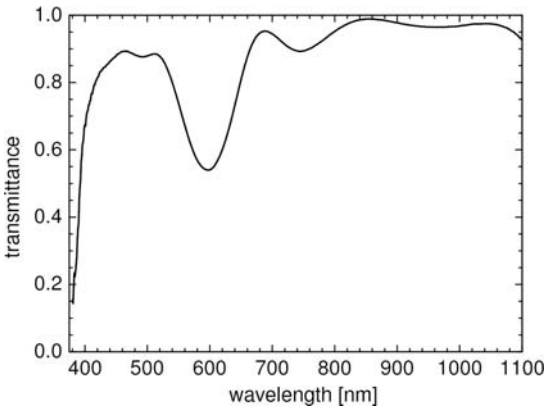

Figure 24 Integrated transmittance of the sample ZnO inverted opal on glass onto a silicon solar cell. Photonic band stop filtering is observed, a very high transmittance through the sample measured between 700 and 1100 [30].

We can clearly identify the main drop in transmittance, caused by the photonic stop gap at about 600 nm wavelength. The amplitude drops down to about 52% there. Also the onset of absorption from the zinc oxide can be identified: at the short wavelength flank transmittance drops steeply, when the ZnO absorbs high energy photons. The reduced transmittance in at short wavelengths is not a problem, as the absorption in a-Si is very efficient there. The long wavelength range shows high transmittance, with an average value of 95.7% between 700 nm and 1100 nm. The thin-film oscillations turn out to be much weaker than in coherent simulations and even lower than in specular reflection spectroscopy. The reduction of transmittance by the photonic stop gap however, turns out to be also less pronounced than one would have expected from the reflectance measurements, but is still about 40%.

7.2 Solar cell integration To combine the inverted opal IRL with a micromorph tandem cell, we took the first step of growing the opal template on the backside of an a-Si:H top cell. The fabrication process runs top to bottom, starting with the front glass, ending with the back contact. The cell is therefore of so-called superstrate type, directly deposited on the ZnO coated front glass. Our structure consists of $d = 360$ nm air spheres surrounded by undoped ZnO from ALD. The PMMA template removal was forced by alternating cycle of bathing in a heated THF liquid/vapour phase environment and careful tempering. On the backside of the finalized PhC interlayer was then deposited a thin layer of silicon, to produce the correct optical interface with the bottom junction of a tandem cell. The sample was terminated with a metal back contact. This sandwich structure is shown in Fig. 25.

To verify that the fabricated device works properly, its quantum efficiency has been measured in the visible spectrum. The resulting graph is shown in Fig. 26.

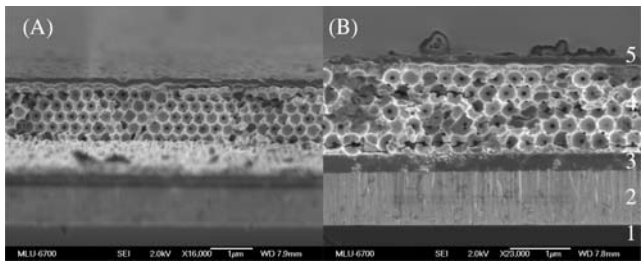

Figure 25 SEM micrographs of a cleaved edge from IRL prototype sample: (A) the inv. opal film covers the back of the a-Si cell. (B) The layers consist of (1) glass, (2) p-type and intrinsic a-Si, (3) n-type a-Si, (4) 3D photonic IRL of ZnO and (5) Si backside. The sample is terminated by a thin metal contact.

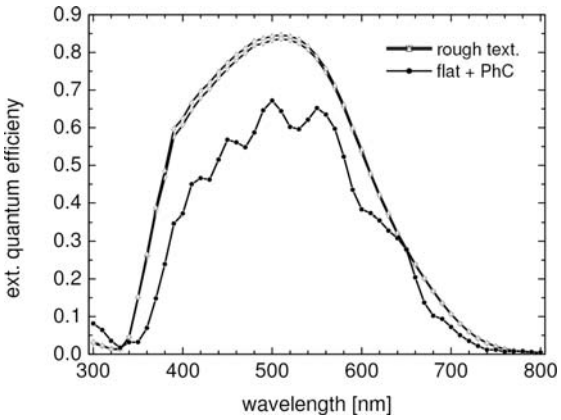

Figure 26 Experimental EQE data of the flat a-Si:H cell with PhC reflector at the backside and two reference cells of textured a-Si:H. The textured cells produce far better EQE, while the flat cell shows typical Fabry–Perot oscillations from the flat interfaces. The fabricated device is obviously optically limited in its light-trapping capabilities and stays about 10%–20% below the reference cell's EQEs.

The EQE has been measured at reverse bias voltage. The bias influence has been observed to saturate between 2 V and 3 V, which was interpreted as a large series resistance in the IRL. In comparison to two highly efficient reference cells with randomly textured light-trapping front, the flat cell with the PhC suffers over nearly the complete absorption region from reduced absorbance. Nevertheless have these first experiments shown the compatibility of the proposed device with micromorph thin-film technology. Also they identified two important device parameters: the conductivity of the IRL and the need for a light-trapping component in the cell.

7.3 Random rough superstrate As the randomly rough surface of HCl etched ZnO on the front glass is currently the best available light trapping structure for the tandem, the possibility to grow an opaline IRL directly on this conformal roughness would allow a direct introduction of our device in the fabrication process of the micromorph tandem. This is not only a desired option, but a necessary condition to avoid additional planarization steps of a rough superstrate cell to allow the PhC growth: because of the importance of textured front contacts in light trapping for thin-film cells, it not possible to abandone it for an IRL. Unfortunately, opal films are typically grown either on patterned substrates to improve the lattice quality or force certain orientations – or on perfectly flat substrates. From experience, opal growth on rough substrates usually leads to disordered, amorphous colloidal films. This appears at first sight to be a fundamental problem that could prevent the application of our self-organized PhC films to the existing tandem cell technology. Our growth experiments on the actual superstrate top-cells however show, that the self-organization process is capable of healing out the distor tion caused by they silicon substrate roughness within certain limits. After a sufficiently large number of opal layers, the fcc structure will prevail. In Fig. 27, an opal film on a textured a-Si:H substrate (top cell back side) is shown.

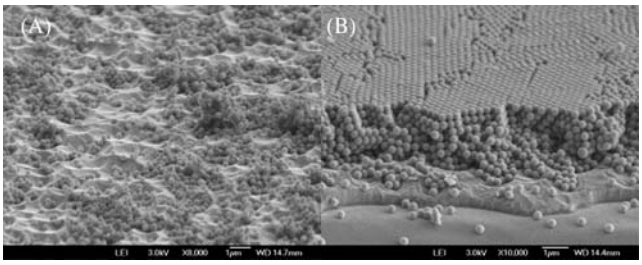

Figure 27 Micrographs of PMMA opal template grown on textured a-Si thin film back side: (A) amorphously arranged colloidal nano spheres at the bottom, (B) organized growth in the upper region of ~10 layer film. Sphere diameter is $d = 298$ nm.

The disordered bottom of opal growth in contact with the roughness can be seen in Fig. 27(A), as well as the crystalline phase that develops within only a few layers, Fig. 27(B).

The feasiblility of opal thin-film growth on a randomly textured silicon surface has therefore been shown. It allows us to combine our photonic device with the existing light-trapping technology, which is a key feature to successful application.

To characterize the optical quality of this perturbed photonic crystal thin-film, we performed comparative transmittance measurements under a microscope, fiber-coupled to a photodiode-array equipped spectrometer. At magnifications of $M = 20$ ($NA = 0.3$), we compared the transmittance of the unprocessed textured a-Si substrate with the transmittance of the same sample with the opal template on top of it. Therefore, light hits the superstrate glass first, passes through the textured ZnO front TCO and the thin conformal a-Si layer (of only 80 nm thickness here), before it interacts with the PhC. The impact of the PhC in this sandwich structure can be seen in Fig. 28.

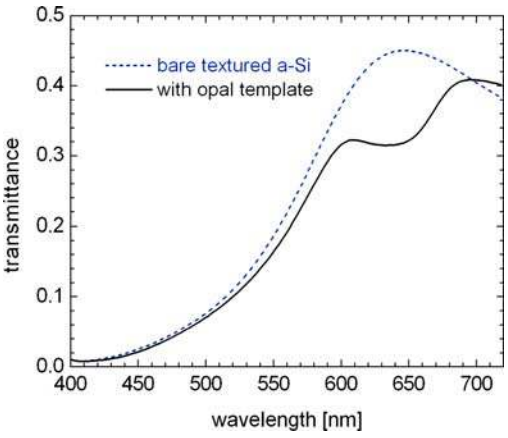

Figure 28 (online colour at: www.pss-a.com) Transmittance of the thin a-Si cell with a back-side opal film (solid) and without (dashed) for comparison. The stop gap at about 640 nm is clearly observed.

The measured transmittance in the microscope is limited by the numerical aperture of the objective to about 0.5 for these samples, due to the highly efficient scattering at the rough texture. The onset of absorption of the a-Si film and its characteristic slope are affected by the opal band stop filtering around 640 nm in wavelength. The relative decrease of transmittance is 30% at 642 nm. Although the disorder introduced by the texture has decreased the film quality, as observed in SEM investigations, the photonic stop gap has nevertheless developed. Transmittance experiences a small decrease at shorter wavelegths than the stop gap position. This loss is attributed to scattering processes at crystal defects in the PhC, as its ratio is increasing with wavelength.

Although randomness in a photonic crystal is usually a problem, we may again benefit from a certain disorder. The Bragg reflection peaks of opal films are known to decrease in amplitude if a film possesses less crystalline order. But it also changes its width to larger values. With an appropriate control of the growth procedures, it should be feasible to affect also the spectral width and reflectance amplitude by changing the 'quality' of the template.

8 Conclusion We have investigated the potential, impact and experimental fabrication of 3D photonic intermediate filters for tandem solar cells, with focus on micromorph tandem cells. Our approach makes use of self-organized growth of colloidal crystals, which is suited for up-scaling and low-cost fabrication. An application in between two junctions requires certain optical properties. With use of polymeric opal templates and zinc-oxide inversion processes, we fabricated the proclaimed structures. The desired spectral peculiarities were verified in optical analysis of our photonic crystals. They show the desired spectrally selective reflectance spectrum with a limited, but sufficiently large spectral width. The necessary long pass filtering in transmittance has been verified to 95% between 700 nm and 1100 nm. Here, additional losses for the bottom cell can be eliminated. All photonic properties can be finely tuned by changes in the template lattice and the TCO infiltration. Also, the samples show a very low effective index of refraction because of the low filling fractions of the high indexed TCO. This can be an advantage for their task as reflectors between the silicon cells and enhances the internal reflection in the silicon junctions. With the use of (undoped) zinc oxide, a typical TCO in solar energy applications, we are already close to the desired order of magnitude for electrical conductivity. Initial steps towards integration into a solar cell have been explored and the very first realization of an internal photonic reflector has been demonstrated: a prototype photonic crystal intermediate reflector at the back of an a-Si:H top cell has been prepared and characterized via quantum efficiency measurements. Thus, the technological compatibility has been shown. Also the compatibility with rough substrates has been proven experimentally, allowing for the combination of our photonic crystal with the randomly textured superstrate technology of micromorph tandem cells.

Acknowledgements We would like to thank C. Stehr for her work in colloid synthesis and Dr. B. Lange for his preliminary contributions in vapour deposition processing. The authors gratefully acknowledge the financial support from the German science foundation (DFG) under Pak88.

References

[1] H. Nagel, A. G. Aberle, and R. Hezel, Prog. Photovolt., Res. Appl. **7**, 245–260 (1999).
[2] S. Lo, C. Chen, F. Garwe, and T. Pertsch, J. Phys. D, Appl. Phys. **40**, 754–758 (2007).
[3] K. R. Catchpole and M. A. Green, J. Appl. Phys. **101**, 063105 (2007).
[4] Y. Su, W. H. Fen, Z. H. Li, D. Wu, and Y. H. Sun, Appl. Opt. **42**(1), 106–112 (2003).
[5] S. Fahr, C. Rockstuhl, and F. Lederer, Appl. Phys. Lett. **92**, 171114 (2008).
[6] C. Rockstuhl, F. Lederer, K. Bittkau, and R. Carius, Appl. Phys. Lett. **91**, 171104 (2007).
[7] P. Campbell and M. A. Green, Sol. Energy Mater. Sol. Cells **65**, 369 (2001).
[8] H. Stiebig, N. Senoussaoui, C. Zahren, C. Haase, and J. Müller, Prog. Photovolt., Res. Appl. **14**, 13–24 (2006).
[9] C. Heine and R. H. Morf, Appl. Opt. **34**(14), 2476 (1995).
[10] O. Kluth, B. Rech, L. Houben, S. Wieder, G. Schöpe, C. Beneking, H. Wagner, A. Löffl, and H. W. Schock, Thin Solid Films **351**, 247–253 (1999).
[11] D. Duché, L. Escoubas, J. Simon, P. Torchio, W. Vervisch, and F. Flory, Appl. Phys. Lett. **92**, 193319 (2008).
[12] N. Feng, J. Michel, L. Zeng, J. Liu, C. Hong, L. C. Kimerling, and X. Duan, IEEE Trans. Electron Devices **54**(8), 1926–1933 (2007).
[13] D. Inns Lei Shi and A. G. Aberle, Prog. Photovolt., Res. Appl. **16**, 187–194 (2008).
[14] E. Yablonovitch, Phys. Rev. Lett. **58**, 2059–2062 (1987).
[15] P. Bermel, C. Luo, L. Zeng, L. C. Kimerling, and J. D. Joannopoulos, Opt. Express **15**(25), 16986 (2007).
[16] R. H. Morf, Physica E **14**, 78–83 (2002).
[17] M. Green, K. Emery, Y. Hisikawa, and W. Warta, Prog. Photovolt., Res. Appl. **15**, 425–430 (2007).
[18] M. Green, Third Generation Photovoltaics (Springer, Berlin, 2003).
[19] T. Repmann, J. Kirchhoff, J. Reetz, F. Birmans, J. Müller, and B. Rech, Conference Record of the 3rd World Conference on PV Energy Conversion, 2003.
[20] M. N. Van den Donker, A. Gordijn, H. Stiebig, F. Finger, B. Rech, B. Stannowski, R. Bartl, E. A. G. Hamers, R. Schlatmann, and G. J. Jongerden, Sol. Energy Mater. Sol. Cells **91**, 572–580 (2007).
[21] B. Rech, J. Müller, T. Repmann, O. Kluth, T. Roschek, J. Hüpkes, H. Stiebig, and W. Appenzeller, Mater. Res. Soc. Symp. Proc. **762**, A3.1 (2003), ISBN 1-55899-699-0.
[22] D. Dominé, J. Steinhauser, L. Feitknecht, A. Shah, and C. Ballif, Conference Record of the 4th IEEE World Conference on PV Energy Conversion, 2006, Vol. 3, pp. 1465–1468.

[23] P. Buehlmann, J. Bailat, D. Dominé, A. Billet, F. Meillaud, A. Feltrin, and C. Ballif, Appl. Phys. Lett. **91**, 143505 (2007).
[24] S. Johnson and J. Joannopoulos, Opt. Express **8**(3), 173–190 (2001).
[25] K. Yamamoto, A. Nakajima, M. Yoshimi, T. Sawada, S. Fukuda, T. Suezaki, M. Ichikawa, Y. Koi, M. Goto, T. Meguro, T. Matsuda, T. Sasaki, and Y. Tawada, Conference Record of the 2006 IEEE 4th World Conference on PV Energy Conversion, 2006, Vol. 2, pp. 1489–1492.
[26] F.-J. Haug et al., Proc. 7th Int.l PV Solar Energy Conf., Fukuoka, Japan, 2008.
[27] J. Krc, F. Smole, and M. Topic, J. Non-Cryst. Solids **352**, 1892–1895 (2006).
[28] A. Bielawny, P.-T. Miclea, R. B. Wehrspohn, A. v. Rhein, C. Rockstuhl, M. Lisca, F.-L. Lederer, B. Lange, R. Zentel, and R. Carius, Proc. SPIE **6651**, 665106 (2007).
[29] D. M. Whittaker and L. S. Culshaw, Phys. Rev. B **60**(4), 2610–2618 (1999).
[30] A. Bielawny, P.-T. Miclea, R. B. Wehrspohn, S. M. Lee, M. Knez, C. Rockstuhl, M. Lisca, F.-L. Lederer, and R. Carius, Proc. SPIE **7002**, 700208 (2008).
[31] M. Egen and R. Zentel, Macromol. Chem. Phys. **205**, 1479 (2004).
[32] M. Egen, R. Voss, B. Griesebock, and R. Zentel, Chem. Mater. **15**, 3786 (2003).
[33] M. Müller, R. Zentel, T. Maka, S. G. Romanov, and C. M. Sotomayor Torres, Chem. Mater. **12**, 2508 (2000).
[34] D. Allard, B. Lange, F. Fleischhaker, R. Zentel, and M. Wulf, Soft Mater. **3**(2/3), 121 (2006).
[35] B. H. Juarez, P. D. Garcia, D. Golmayo, A. Blanco, and C. Lopez, Adv. Mater. **17**, 2761 (2005).
[36] B. Lange, F. Fleischhaker, and R. Zentel, Macromol. Rapid Commun. **28**, 1291 (2007).
[37] M. Egen, Funktionale dreidimensionale Photonische Kristalle aus Polymerlatizes, Ph.D. thesis, Mainz (2003).
[38] J. F. Bertone, P. Jiang, K. S. Hwang, D. M. Mittleman, and V. L. Colvin, Phys. Rev. Lett. **83**, 300 (1999).

